Supporting information on 'Measurement report: Chemical composition of submicron aerosol and cirrus and contrail ice residuals measured in the UTLS over Germany in winter 2018'

Philipp Brauner[1,*], Oliver Appel[1,*,2], Oliver Eppers[1,*], Franziska Köllner[1,*,2], Hans-Christian Clemen[1,*], Tiziana Bräuer[3], Hans-Christoph Lachnitt[2], Katharina Kaiser[1,*], Johannes Schneider[1,*], Antonis Dragoneas[4], Andreas Hünig[1,8], Sergej Molleker[5], Bruce E. Anderson[6], Yafang Cheng[7,*], Hans Schlager[3], Christiane Voigt[2,3], and Stephan Borrmann[1,2]

[1]Particle Chemistry Department, Max Planck Institute for Chemistry, Mainz, Germany
[2]Institute for Physics of the Atmosphere, Johannes Gutenberg University, Mainz, Germany
[3]Institute of Atmospheric Physics, Deutsches Zentrum für Luft- und Raumfahrt (DLR), Oberpfaffenhofen, Germany
[4]Climate Geochemistry Department, Max Planck Institute for Chemistry, Mainz, Germany
[5]Instrument Development and Electronics Department , Max Planck Institute for Chemistry, Mainz, Germany
[6]NASA Langley Research Center (LaRC), Hampton, USA
[7]Multiphase Chemistry Department , Max Planck Institute for Chemistry, Mainz, Germany
[8]now at: SCHOTT AG, Mainz, Germany
[*]now: Aerosol Chemistry Department, Max Planck Institute for Chemistry, Mainz, Germany

Correspondence: Stephan Borrmann (stephan.borrmann@mpic.de)

S1 The hybrid mass spectrometer ERICA

The measurements of the aerosol chemical composition were conducted using the hybrid mass spectrometer ERICA (ERC Instrument for the Chemical composition of Aerosols; Hünig, 2020; Hünig et al., 2022; Dragoneas et al., 2022) which consists of two individual mass spectrometer, the ERICA-LAMS and ERICA-AMS. The ERICA-LAMS (laser ablation mass spectrometer) is based on the laser desorption and ionization technique (LDI) and a subsequent time-of-flight mass spectrometer (TOF-MS) (e.g., Hinz et al., 1994; Prather et al., 1994; Johnston and Wexler, 1995; Murphy and Thomson, 1995; Suess and Prather, 1999; Zelenyuk and Imre, 2005). The instrument is used for the analysis of single particles in a size range of 170 nm to 3.2 $\mu\mathrm{m}$ (Hünig, 2020). The ERICA-AMS (aerosol mass spectrometer) implements the thermal desorption and ionization technique for bulk measurements of ensembles of particles ranging from 80 nm to 2 $\mu\mathrm{m}$ (Hünig et al., 2022). The method was first deployed in the Aerodyne AMS and is described in Drewnick et al. (2005) and Canagaratna et al. (2007). Both mass spectrometers share one vacuum chamber, allowing for the parallel sampling of the same air mass. The hybrid system was introduced in detail by Hünig et al. (2022) and Dragoneas et al. (2022) and is briefly described here: The sample air is provided to the inlet system of ERICA, consisting of a constant pressure inlet (CPI, Molleker et al., 2020) and an aerodynamic lens. In order to maintain a constant mass flow rate of 1.45 $\mathrm{cm^3 s^{-1}}$ (under normal temperature and pressure conditions NTP: 20 $^{\circ}\mathrm{C}$ and 1013.25 hPa) into ERICA, the CPI was set up as a pinch device which compresses an in-house made silicone O-ring. In consequence, the critical orifice of the inlet line is adaptable for variable atmospheric pressure regimes from 1000 to 50

Table S1. Overview of the parameters applied for the fuzzy c-means clustering of the ND-MAX dataset. Subclustering and sub-subclustering were applied to the cluster of non-assigned mass spectra of the previous clustering routine.

Parameter	Main clustering	Sub-clustering	Sub-sub-clustering
Number of cluster	50	20	20
Type of clustering	fuzzy c-means	fuzzy c-means	fuzzy c-means
Initialization type	find different startcluster	find different startcluster	find different startcluster
Source for clustering	anion + cation	cation	cation
Normalization type	sum	sum	sum
Normalization time	before and after concatenation	after concatenation	after concatenation
Startcluster difference	0.8	0.3	0.7
Pre-processing type	power each mz	power each mz	power each mz
Pre-processing power	0.5	0.5	0.5
Fuzzifier	1.7	1.2	1.2
Fuzzy abort	0.001	0.001	0.1
Distance mode	correlation	correlation	correlation

hPa and provides a pressure of 4.53 hPa at the aerodynamic lens (Appel et al., 2022). Accelerated into the vacuum chamber, the aerosol particles enter the ERICA-LAMS section passing two consecutive detection lasers (150mW UV-laser of 405 nm wavelength each) before they reach the ablation spot. The travel time between both detection lasers is used to infer the particle size and to trigger a pulsed ablation laser (UV laser of 10.9 mJ pulse energy at a wavelength of 266 nm, in total 44 mJ) in order to desorb and ionize the individual particles as soon as the ablation spot is reached. A calibration with particles of known diameter, density, and shape (Hünig et al., 2022) allows for the derivation of the vacuum-aerodynamic diameter of the particles (d_{va}) from the recorded particle velocity between both detection stages. The LDI technique is similar to the ALABAMA (Brands et al., 2011) and PALMS (Murphy, 2007). The ionized components of the ablated particles are extracted and accelerated into the ToF-MS by switched electrical fields. The majority of particles continue their way into the ERICA-AMS as they are not ablated due to a limited firing frequency of the UV laser (idle time > 120 ms). There, the particles impact on a tungsten heater body of 600 $^{\circ}\mathrm{C}$ and are flash-vaporized. An electron beam is released from a heated tungsten filament by thermionic emission (Kellner et al., 2004) and ionizes the cloud of vaporized particles. The resulting cations are extracted periodically into the compact ToF-MS (Hünig et al., 2022), providing unipolar positive mass spectra of particle ensembles (Appel et al., 2022).

S2 Particle Clustering

The entire dataset of 54403 mass spectra obtained with the ERICA-LAMS was clustered using the fuzzy c-means algorithm (Bezdek et al., 1984; Hinz et al., 1999). The clustering routine was followed by two subsequent sub-clustering routines to

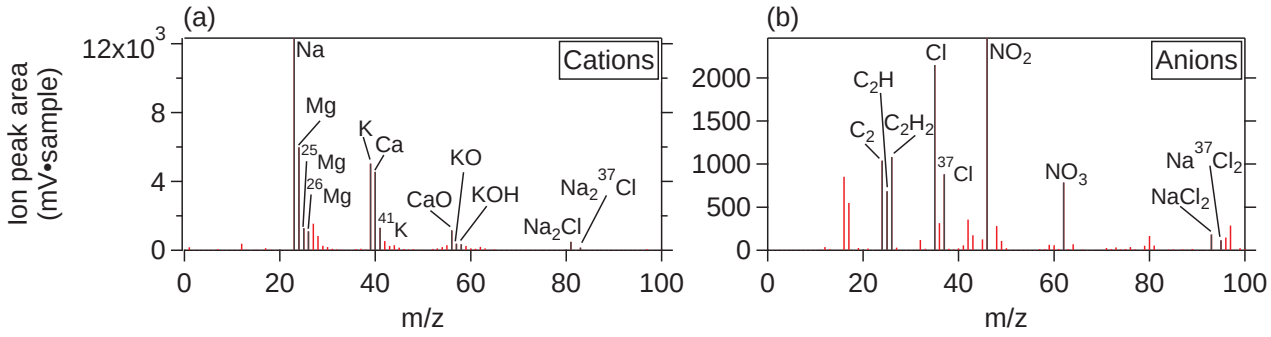

Figure S1. Mean mass spectrum of cations (a) and anions (b) for sea spray particles detected by ERICA-LAMS during ND-MAX.

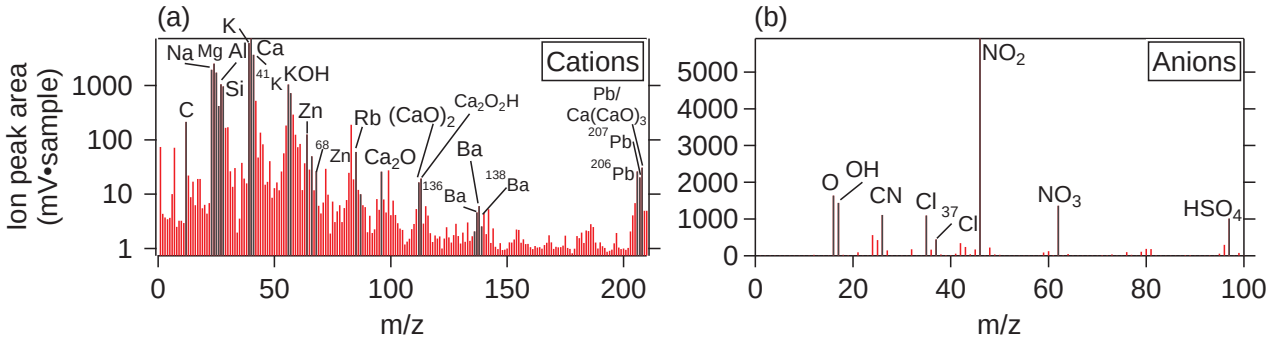

Figure S2. Mean mass spectrum of cations (a) and anions (b) for processed sea spray particles detected by ERICA-LAMS during ND-MAX. Note the logarithmic axis scaling for cations that was chosen due to the particularly high potassium cation signal.

minimize the number of undefined mass spectra. The settings applied for the fuzzy c-means clustering are provided in Table S1. A detailed description of the parameters is given in Brauner (2024). Table S2 provides an overview of the inorganic particle types that were obtained by the clustering procedure. Table S3 lists all carbon-containing and organic particle types detected during ND-MAX. Further, the ion marker peaks of their mean mass spectra are named and interpreted using corresponding references. The mean mass spectra of the particle types obtained by the particle clustering are presented in Fig. S1 to S12.

S3 Definition of particle-related events

The dataset of ND-MAX was divided into several periods of interest based upon the number concentrations of aerosol and ice particles as well as the volume mixing ratio of carbon dioxide. In order to analyze the atmospheric background, aircraft exhaust, cirrus, and contrail events, the mentioned parameters were examined for periods of enhancement: For the derivation of ice particle events, the ice particle number concentration was proven to exceed the threshold of background noise for each time

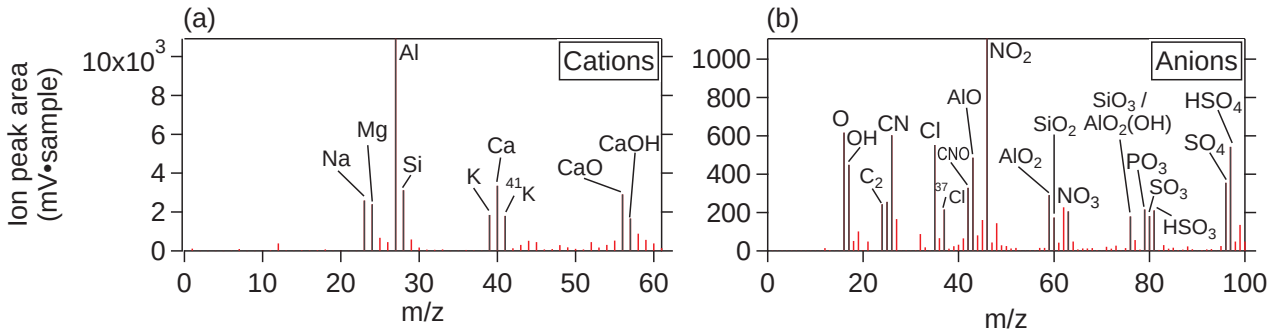

Figure S3. Mean mass spectrum of cations (a) and anions (b) for mineral dust particles detected by ERICA-LAMS during ND-MAX.

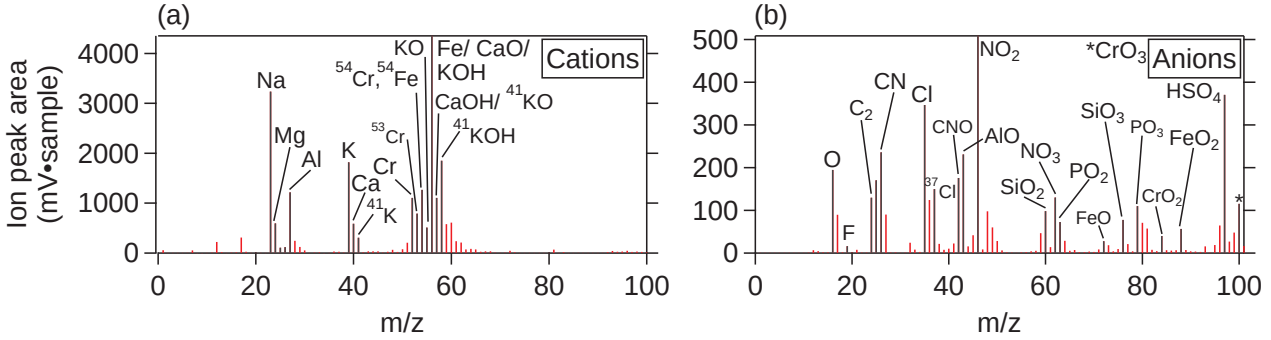

Figure S4. Mean mass spectrum of cations (a) and anions (b) for processed mineral dust particles detected by ERICA-LAMS during ND-MAX.

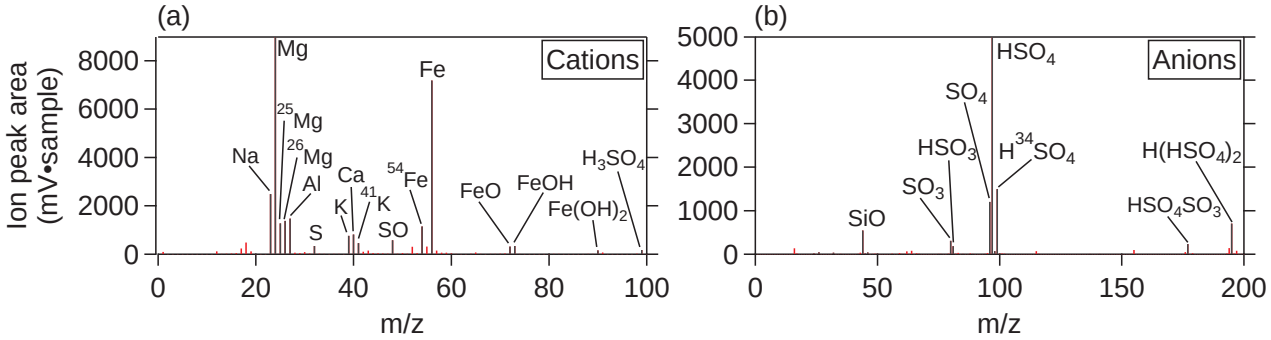

Figure S5. Mean mass spectrum of cations (a) and anions (b) for particles of meteoric material detected by ERICA-LAMS during ND-MAX.

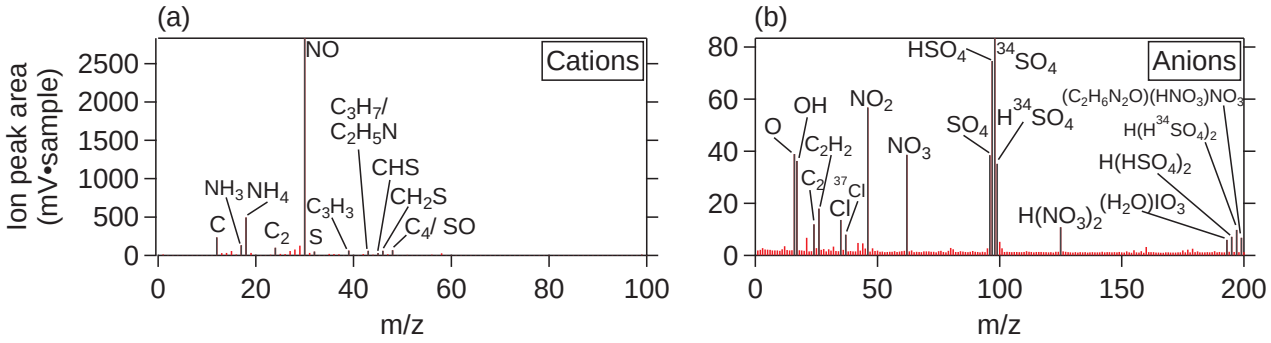

Figure S6. Mean mass spectrum of cations (a) and anions (b) for nitrogen-rich particles detected by ERICA-LAMS during ND-MAX.

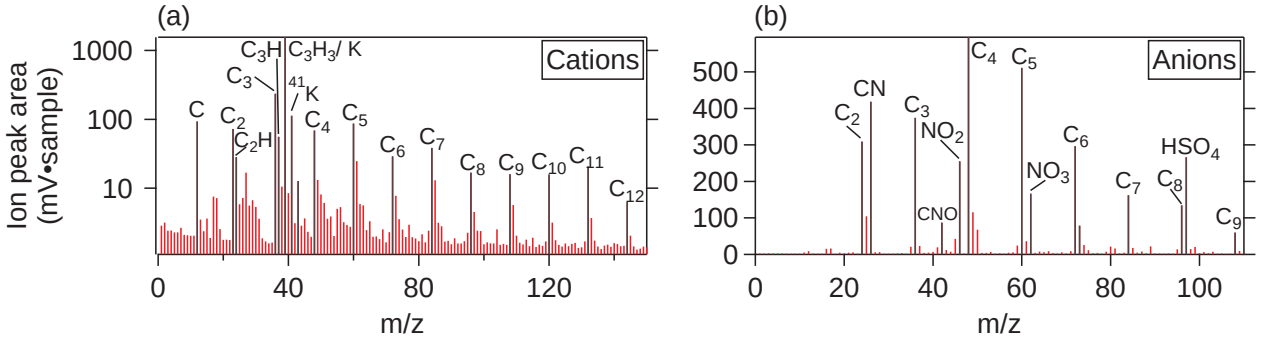

Figure S7. Mean mass spectrum of cations (a) and anions (b) for EC/ soot particles detected by ERICA-LAMS during ND-MAX. Note the logarithmic axis scaling for cations that was chosen due to the particularly high potassium cation signal.

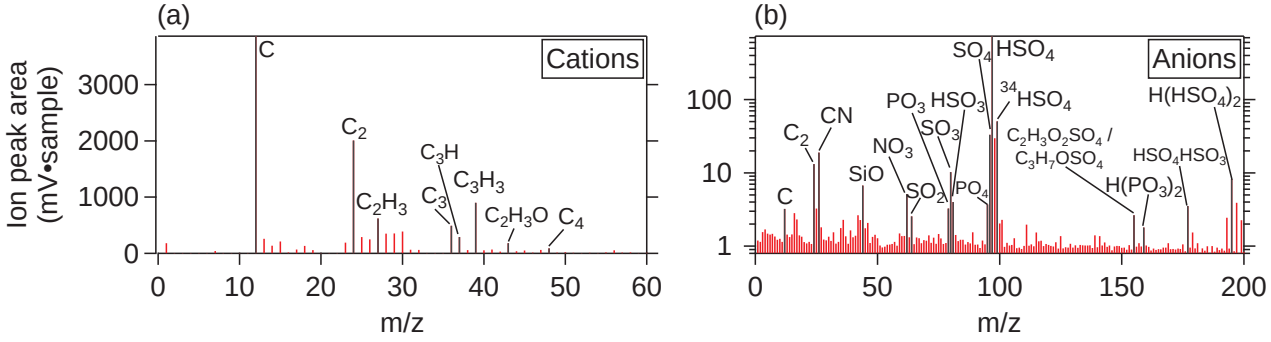

Figure S8. Mean mass spectrum of cations (a) and anions (b) for coated soot particles detected by ERICA-LAMS during ND-MAX. Note the logarithmic axis scaling for anions that was chosen due to the particularly high sulfate anion signal.

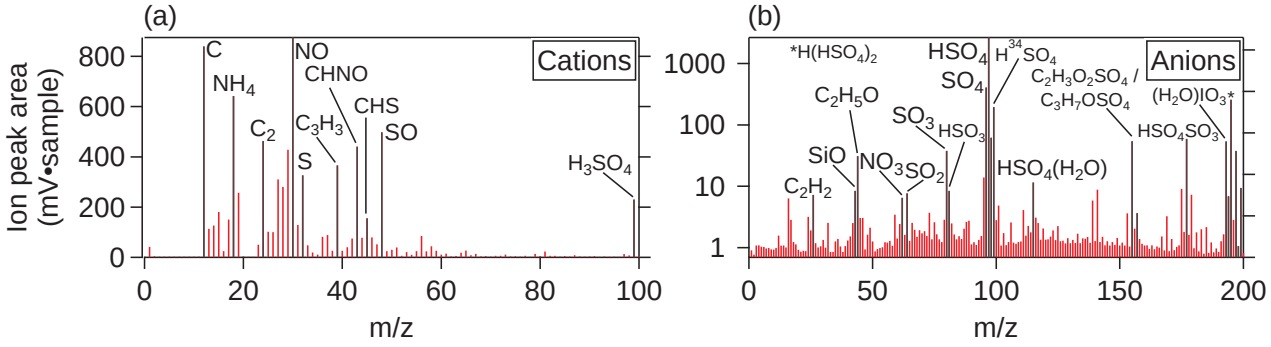

Figure S9. Mean mass spectrum of cations (a) and anions (b) for processed ECOC particles detected by ERICA-LAMS during ND-MAX. Note the logarithmic axis scaling for anions that was chosen due to the particularly high sulfate anion signal.

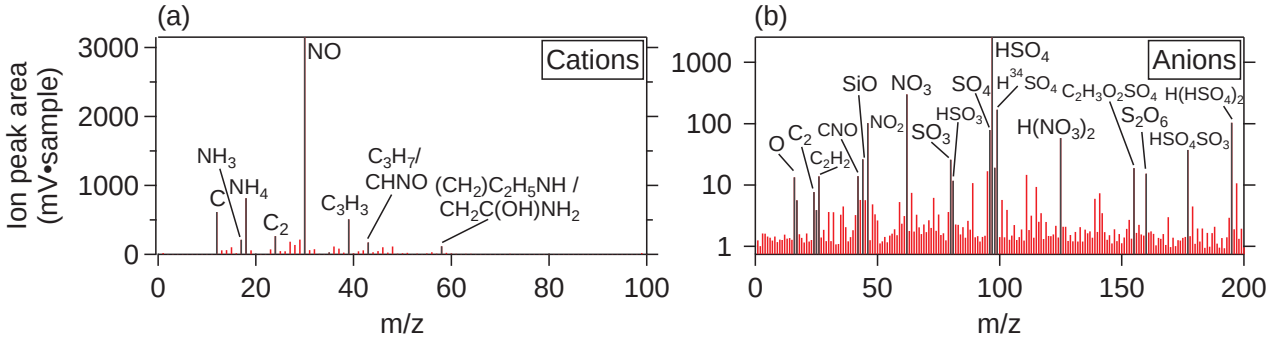

Figure S10. Mean mass spectrum of cations (a) and anions (b) for processed OC particles detected by ERICA-LAMS during ND-MAX. Note the logarithmic axis scaling for anions that was chosen due to the particularly high sulfate anion signal.

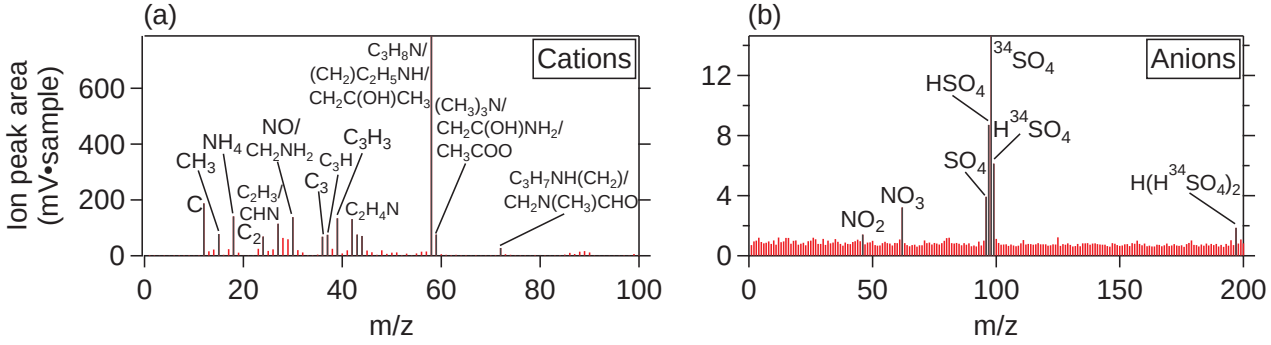

Figure S11. Mean mass spectrum of cations (a) and anions (b) for amine particles detected by ERICA-LAMS during ND-MAX.

Table S2. Overview of the classified inorganic particle types detected by ERICA during the ND-MAX campaign, including their predefined names, ion-marker-peaks, and literature for interpretation.

Particle type	**Ion marker peaks** (m/z)	**Literature/ Comments**
Sea Spray	+23 (Na^+), +24/25/26 (Mg^+), +39/41 (K^+), +40 (Ca^+), +83 (Na_2Cl^+), -35/37 (Cl^-), -93 ($NaCl_2^-$)	Prather et al. (2013); Su et al. (2023)
Processed Sea Spray	same as Sea Spray and +64/66/68 (Zn^+), +85/87 (Rb^+), +136/137/138 (Ba^+), +206/207/208 (Pb^+)	Similar to Sea Spray, including zinc, rubidium, barium, lead Cornwell et al. (2020)
Mineral Dust	+23 (Na^+), +28 (Si^+), +39/41 (K^+), +40 (Ca^+), +54/56 (Fe^+), -60(SiO_2^-), -76 (SiO_3^-)	Silva et al. (2000); Lee et al. (2002); Gallavardin et al. (2008)
Processed Mineral Dust	same as Mineral Dust and +52/53/54 (Cr^+), +56 (Fe^+/CaO^+/KOH^+), -19 (F^-), -35/37 (Cl^-), -42 (CNO^-), -43 (AlO^-), -84 (CrO_2^-), -100 (CrO_3^-)	Similar to Mineral Dust, but also contains fluor, chloride, chrome
Meteoric Material	+23 (Na^+), +24/25/26 (Mg^+), +40 (Ca^+), +54/56 Fe^+), +72 (FeO^+), +73 ($FeOH^+$), -44 (SiO^-), -97/99 (HSO_4^-)	Schneider et al. (2021)

Table S3. Overview of the classified particle types containing carbonaceous material detected by ERICA during the ND-MAX campaign, including their predefined names, ion marker peaks, and literature for interpretation.

Particle type	**Ion marker peaks** (m/z)	**Literature/ Comments**
EC/ Soot	+n· 12 (C_n^+) and -n· 12 (C_n^-) for n=1,...,12	Moffet and Prather (2009); Pratt et al. (2009)
Coated Soot	+n· 12 (C_n^+) for n=1,...,4 and +27 ($C_2H_3^+$), +39 ($C_3H_3^+$), -79 (PO_3^-), -80 (SO_3^-), -97/99 (HSO_4^-)	Moffet and Prather (2009)
Processed ECOC	+12 (C^+), +24 (C_2^+), +18 (NH_4^+), +30 (NO^+), +32 (S^+), +48 (SO^+), +99 ($H_3SO_4^+$), -97/99 (HSO_4^-)	Gunsch et al. (2018)
Proc. OC	+12 (C^+), +18 (NH_4^+), +30 (NO^+), +39 ($C_3H_3^+$), -26 (CN^-/$C_2H_2^-$), -46 (NO_2^-), -62 (NO_3^-), -80 (SO_3^-), -97/99 (HSO_4^-), -125 ($HN_2O_6^-$)	Pratt et al. (2009)
BB Type I	+12 (C^+), +23 (Na^+), +39/41 (K^+), -46 (NO_2^-), -62 (NO_3^-), -81 (HSO_3^-), -97/99 (HSO_4^-)	Pratt et al. (2009)
BB Type II	BB Type 1 and -25 (C_2H^-), -26 (CN^-), -42 (CNO^-)	Pratt et al. (2009)/ mostly detected in UTLS-region; indication of more organic and more sulfate material compared to BB Type I
Amine	+30 (CH_4N^+), +58 ($C_3H_8N^+$), 59 ($(CH_3)_3N^+$), +70 ($C_4H_10N^+$)	Angelino et al. (2001); Healy et al. (2015)
Nitrogen-rich	+18 (NH_4^+), +30 (NO^+), -46 (NO_2^-), -62 (NO_3^-), -96 (SO_4^-), -97/99 HSO_4^-)	Appel et al. (2022)
Engine Oil	+n· 12 (C_n^+) for n=1,2,3, and +15 (CH_3^+), +27 ($C_2H_3^+$), +37 (C_3H^+), +39 ($C_3H_3^+$), +57 ($C_4H_9^+$), +85 ($C_6H_3^+$), -143 ($C_6H_7O_4^-$), -159 ($H(PO_3)_2^-$)	Clemen et al. (in prep.)

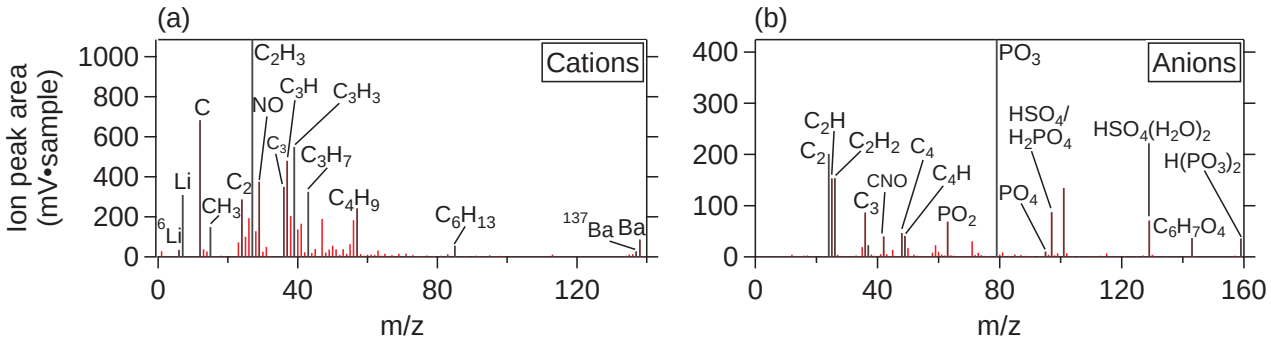

Figure S12. Mean mass spectrum of cations (a) and anions (b) for engine oil particles detected by ERICA-LAMS during ND-MAX.

step which was found to be 0.35 cm^{-3}. Aerosol particle events, i.e. enhancements in the aerosol particle number concentration were detected by a comparison of the concentration with the mean concentration of the previous 30 s. If the actual value was larger than the mean value including a 3-fold standard deviation, an aerosol particle event was introduced. Equally, this event ended as soon as the actual value fell below the mean concentration of the previous 30 s by 3 times the standard deviation. A similar routine was set up for the determination of CO_2 events. Finally, the individual events were combined in the following way: a combination of an aerosol and CO_2 event is defined as exhaust event (Table S4). A non-event of both, the aerosol number concentration and the CO_2 volume mixing ratio, is referred to as background event. A combination of an exhaust event with an ice particle event and a temperature criterion below -38 °C is referred to as a contrail event. A cirrus event is characterized by an aerosol particle and ice particle event, a background concentration of CO_2 and the temperature criterion as for contrails. A detailed description of the characterization of background periods and air mass events with the help of individual aerosol, trace gas, and ice particle parameters is provided in Brauner (2024).

S4 HYSPLIT analysis

The Hybrid Single-Particle Lagrangian Integrated Trajectory Model (HYSPLIT), developed by the American NOAA and Australia's Bureau of Meteorology was applied for the simulation of backward air mass trajectories along the flight path. The model ran in the desktop version v5.2.1 with a set of operational data of 0.5° resolution from the Global Data Assimilation System (GDAS) of the American National Centers for Environmental Prediction (NCEP). Trajectories were calculated for every RF starting at the GPS position of the NASA DC-8 aircraft and traced back up to 10 days in the time, resulting in a total of 2670 trajectories and 240 time steps per trajectory (one point every hour). In order to trace back BB Type I to the Thomas Fire, the contribution of the Pacific US Coast region (25°–40° N, 140°–110° W) to the air masses sampled along the flight track was compared with the occurrence of BB Type I during the RFs. Since the HYSPLIT model reveals an irregular behavior at the boundary areas, some trajectories have to be excluded from the interpretation: Backward trajectories starting 50 m a.s.l. tend to stay in the boundary layer (BL) and touching the ground. Trajectories reaching back to the lowermost 50 m for a time frame

Table S4. Overview of the particle-related events and their criteria.

Event	Criteria	Inlet system
Atmospheric background	background aerosol number concentration, background CO_2 volume mixing ratio	Scoop
Aircraft exhaust plume	enhanced aerosol number concentration, enhanced CO_2 volume mixing ratio	Scoop
Cirrus	enhanced aerosol number concentration, background CO_2 volume mixing ratio, enhanced ice particle number concentration, T < -38 °C	CVI
Contrail	enhanced aerosol number concentration, enhanced CO_2 volume mixing ratio, enhanced ice particle number concentration, T < -38 °C	CVI

of more than 12 hours are terminated and not traced back any longer. They adapt to the properties of the BL they have passed before reaching the aircraft. Further, a certain fraction of trajectories tend to leave the model frame by ascent into the upper stratosphere and is, thus, neglected. Finally, trajectories that never crossed the BL are disregarded since they do not provide any information about the air mass origin.

HYSPLIT only provides data of relative humidity with respect to water. In order to derive the relative humidity concerning the ice phase, we use the proportion of the water vapor partial pressure e and the saturation pressure of water vapor with respect to ice $e_{s,ice}$.

$$RH_{ice} = \frac{e}{e_{s,ice}} \tag{S1}$$

The partial pressure is calculated using the ideal gas equation for water vapor including the density of water vapor ρ_{H_2O}, ideal gas constant for water vapor R_{H2O} and the temperature T. The equation is transformed to include the parameters provided by HYSPLIT: the water vapor mass mixing ratio w and the pressure p. The mole fraction is defined by the molar mass of dry air ($M_{dry} = 28.96$ g mol^{-1}) and of water vapor ($M_{H_2O} = 18.01258$ g mol^{-1}).

$$e = \rho_{H_2O} \cdot R_{H_2O} \cdot T = w \cdot p \cdot \frac{M_{dry}}{M_{H_2O}} \tag{S2}$$

The saturation pressure e_s is calculated according to Murphy and Koop (2005). The factor of 1/100 is the conversion factor for hectopascal.

$$e_s = \frac{1}{100} \cdot exp(9.550426 - \frac{5723.265}{T} + 3.53068 \cdot ln(T) - 0.00728332 \cdot T) \tag{S3}$$

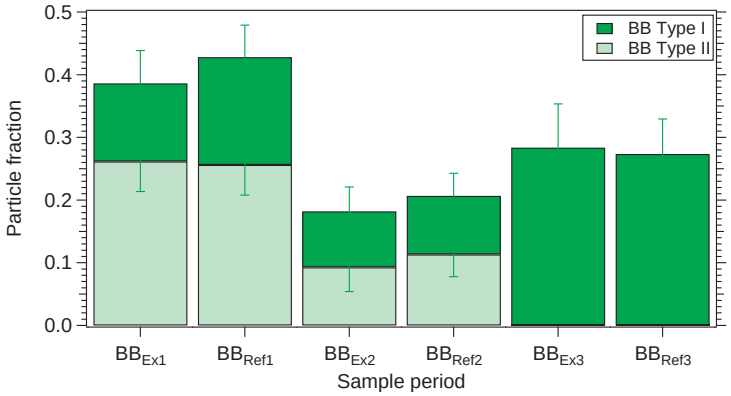

Figure S13. Relative abundance of BB particles for three samples of exhaust (Ex1–Ex3) and corresponding background reference (Ref1–Ref3) periods: BB$_{Ex1}$: RF1, 13:12:57–13:17:46 UTC, BB$_{Ref1}$: RF1, 13:05:00–13:09:49 UTC, BB$_{Ex2}$: RF8, 10:44:50–10:49:51 UTC, BB$_{Ref2}$: RF8, 10:38:00–10:43:01, BB$_{Ex3}$: RF5, 13:33:29–13:37:39 UTC, and BB$_{Ref3}$: RF5, 13:25:00–13:29:10 UTC. The error bars illustrate the uncertainty of the particle fraction as a result of the binomial counting statistics (Sect. S7).

S4.1 Examples of airmass-induced variability of BB particles

The comparison of cirrus and contrail residuals suggest that particles of BB Type I might result from aircraft exhaust as a consequence of fuel blends partly consisting of biofuels (Fig. 14b). However, the particle fraction of biomass burning material is much more affected by the background air mass than by the emission of aircraft exhaust. Figure S14 provides a detailed overview of the sample periods presented in Fig. 8, differing between periods of atmospheric background (BB$_{Ref1-3}$) and of aircraft exhaust plumes (BB$_{Ex1-3}$) in a short time frame next to each other to provide comparable atmospheric conditions. The relative occurrence of both BB Types is very similar for exhaust and background periods measured next to each other. In contrast, the occurrence of the particle types is more variable between the individual background periods of different RFs, implying that the presence of both BB Types is driven by the atmospheric background air mass history and not by aircraft emissions.

S4.2 Oxidative aging of BB Type I and BB Type II

In order to prove the oxidative aging of the BB Types I and II, the ratios of f_{44} and f_{43} were determined by complementary data of the organic particulate matter detected with the ERICA-AMS. Figure S15 depicts the ratio of f_{44} and f_{43} for every single particle of BB Type I and II as well as their median and quartiles. f_{44} is defined as the ratio of the m/z 44 signal to the total signal in the organic-spectrum, f_{43} is analogously defined for m/z 43. The ratio of f_{44} to f_{43} is used to differ between hydrocarbon-like and oxygenated organic aerosol (Ng et al., 2010, 2011). Both particle types show a similar oxidative aging, hindering a further differentiation.

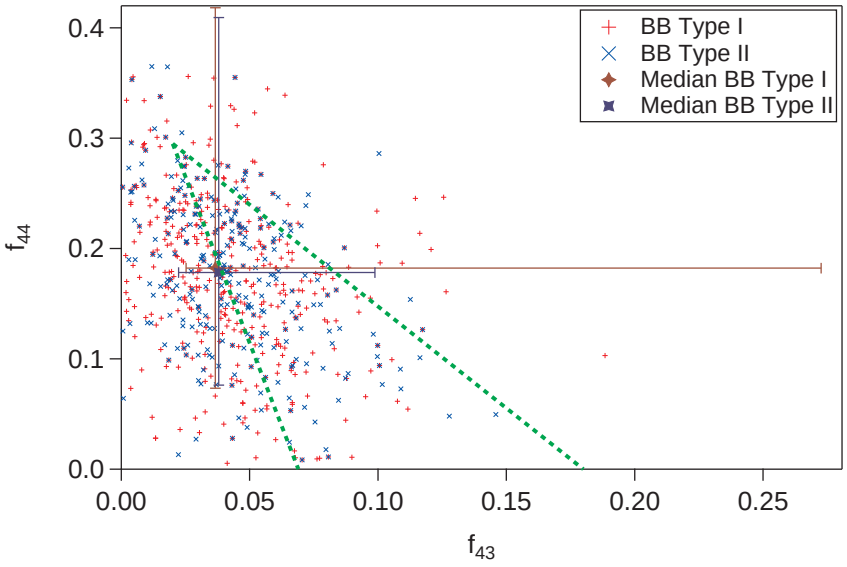

Figure S14. f_{44}-to-f_{43} ratio of BB Type I and II detected with ERICA-LAMS (crosses refer to means of 1 minute) as well as their overall median (displayed as points), 25th and 75th percentile. f_{44} and f_{43} were determined by complementary measurement data of the ERICA-AMS including all RFs except for RF5 and RF6. The green dotted lines refer to the triangular space as introduced by Ng et al. (2010) where oxidized organic aerosol is measured.

S5 Meteorological context

Meteorological conditions were found to play a major role for the presence of individual particle types during the ND-MAX campaign, and thus, had an impact on the chemical composition of aerosol particles in the UTLS region. The prevailing weather pattern affect the vertical profile of different aerosol types. Of originally three prevailing air mass periods (cold, warm, transition air mass period) taking place during ND-MAX, two periods and corresponding meteorological systems were assigned to the RFs discussed in this paper and are discussed in the following.

S5.1 Cold air mass period

RF1, RF2, and RF8 were affected by a cold air mass period. A description of the cold period is provided based on RF1. The meteorological conditions of RF2 and RF8 are introduced in Brauner (2024). On average, the meteorological conditions were characterized by a center of a low pressure system over Northern Europe and a frontal zone which had already passed the measurement region. Figure 10 provides an overview of the temperature fields, high-level dynamics (isophypses), and pressure pattern at mean sea level pressure (isobars) over Europe and the North Atlantic Ocean. The high-level weather map displays a northwesterly atmospheric circulation along the isohypses and isobars, indicating the advection of moist and cold air masses from subpolar regions towards the flight area. In consequence, the temperatures at 850 hPa-level ranged between

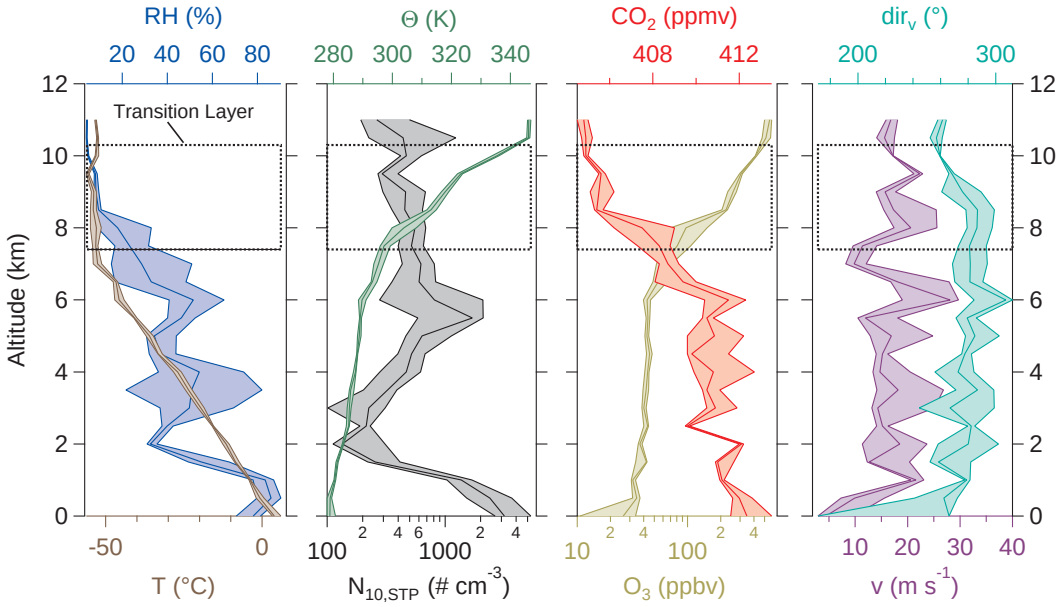

Figure S15. Vertical profiles of meteorological parameters as measured by the NASA DC-8 (RH: Relative Humidity, T: Temperature, Θ: Potential Temperature, v: Wind Speed, dir_v: Wind Direction), volume mixing ratios of O_3, and CO_2, and aerosol particle number concentration ($N_{10,STP}$) for the cold air mass periods during RF1, RF2, and RF8. Medians and interquartile ranges are shown. The black box denotes the vertical extent of the Transition Layer.

-4 and -8°C. Further, the small secondary depression over Poland implies a sector of cold, descending air masses over Central Europe that lead to a subsidence of the local tropopause. The cold air sector provided a well-mixed BL, low-level tropopause, and a westerly circulation as indicated by Fig. S15. Vertically-resolved meteorological parameters besides trace gases and particle number for the cold period are displayed in Fig. S15. The northwestern circulation as indicated by the high-level weather map was confirmed by measurement data of the aircraft ranging between 260 and 300°, which refer to westerly to northwesterly winds. The cold sector provided a lowered tropopause and appendant transition layer above 7 km. Both, the negative temperature gradient and the relative humidity indicate a smooth turnover from tropospheric conditions to a transition region at approximately 7 to 8 km. This transition is also pointed out by trace gas measurements: CO_2 dropped from a level of 411 ppmv to approximately 405 ppmv whereas O_3 increased from tropospheric conditions around 40 ppbv to lowermost stratospheric conditions larger than 100 ppbv.

S5.2 Warm air mass period

RF3, RF4, and RF5 were characterized by a warm air period and pre-frontal meteorological conditions. The features are demonstrated using RF3 as an example. The weather conditions of RF4 and RF5 are described in detail in Brauner (2024). All flights conducted during the warm period were under the impact of similar weather patterns: A moving high-level ridge and an

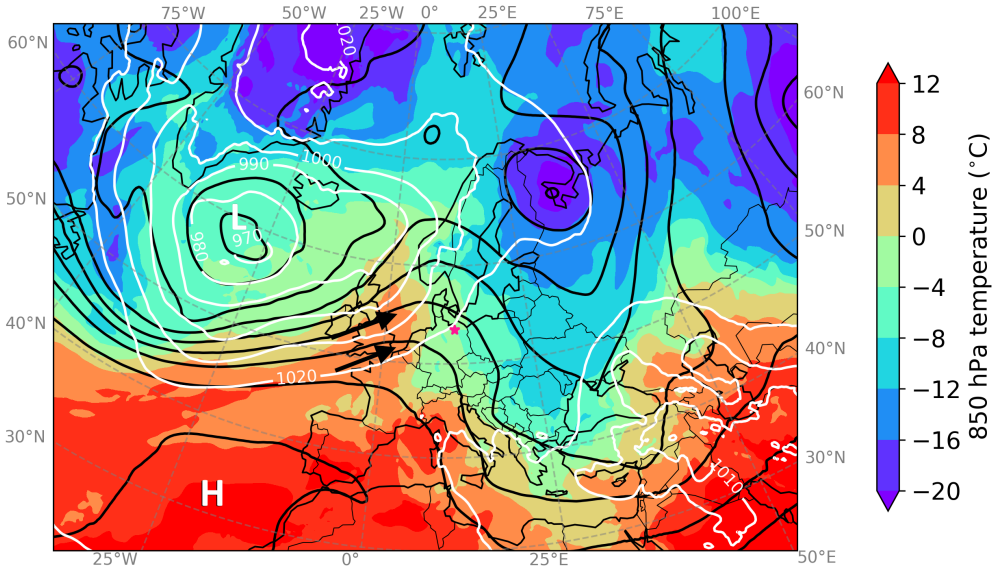

Figure S16. Weather map of 23 January 2018, 12:00 UTC including isohypses at 500-hPa-level (black lines) and mean sea level pressure (white lines), 'H' and 'L' mark the center of high-pressure and low-pressure systems, respectively. The black arrows denote the wind circulation. The color-coding refers to ambient temperatures at the 850-hPa-level and denotes the distribution of warm and cold air masses. The pink star denotes the measurement area of RF1. ERA5 data were provided by Hersbach et al. (2018).

approaching trough of a depression located in the west of the flight area supported the advection of warm air masses towards the flight area. Consequently, temperatures above -4°C at 850 hPa, ascending air masses, and a rise of the local tropopause above 10 km were observed. Figure S16 presents the location of air masses at the 850-hPa-level, high-level dynamics and the pressure pattern at mean sea level pressure. The advection of warm and moist air masses from the southern North Atlantic, attributed to the warm conveyor belt of the approaching low-pressure system, replaced the cold air prevailing during RF1 and RF2 and promoted the formation of cirrus and contrails.

The warm period was characterized by a high-level tropopause above 10 km and the uplift of marine air masses ahead of the frontal zone. Figure S17 provides the vertical profiles of meteorological parameters including trace gases and particle number for the warm period. Although the data recordings did not show a turnover from tropospheric to statospheric conditions, the temperature gradient was slightly reduced above 10.5 km along with a small enhancement of the potential temperature above 10 km, implying the proximity to the tropopause transition layer. This is confirmed by the profile of O_3 above 9.5 km. A relative humidity of around 60 % in the upper troposphere and the increase of particle number concentration towards higher altitudes point out the uplift of air masses as the front approached.

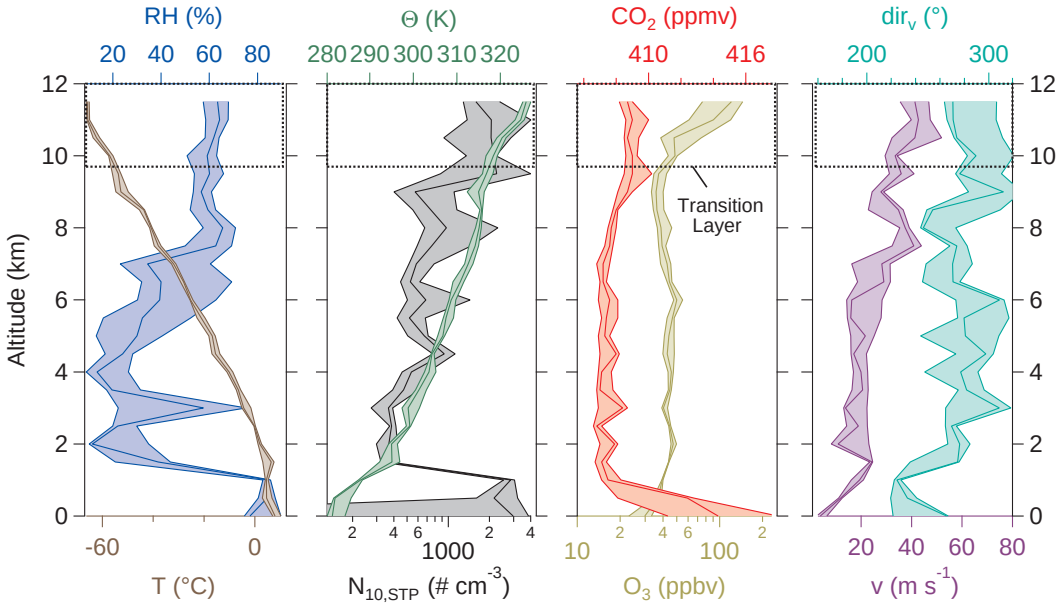

Figure S17. Vertical profiles of meteorological parameters as measured by the NASA DC-8 (RH: Relative Humidity, T: Temperature, Θ: Potential Temperature, v: Wind Speed, dir_v: Wind Direction), volume mixing ratios of O_3, and CO_2, and aerosol particle number concentration ($N_{10,STP}$) for the warm air periods during RF3, RF4, and RF5. Medians and interquartile ranges are shown. The black box denotes the vertical extent of the Transition Layer.

S6 Consistency of ERICA-AMS measurements with complementary AMS-measurements during CAFE-Brazil

The RFs of ND-MAX provided the first opportunity to measure mass concentrations of non-refractory particulate matter over Germany with the ERICA-AMS. Here, we compare the measurement data obtained within the UTLS region over Germany in winter with aerosol measurements of a compact time-of-flight aerosol mass spectrometer (C-ToF-AMS, Aerodyne Research, Inc.) conducted during two test flights for the CAFE-Brazil campaign in late November 2022 and during two transfer flights in late November 2022 and late January 2023 aboard the High Altitude and LOng range research aircraft HALO of the DLR. The measurements provided mass concentrations in a similar range to those conducted within the ND-MAX RFs. The C-ToF-AMS has a similar working principle as the ERICA-AMS including the same optical and vaporizer system, albeit working with a different aerodynamic lens (Schulz et al., 2018). Figure S18 provides a vertical profile of particulate organics, sulfate, ammonium, nitrate, and chloride regarding the mass concentrations. The mass concentrations of organics varied between 0.05 $\mu g\,m^{-3}$ in the free troposphere (FT) and 0.15 $\mu g\,m^{-3}$ in the LMS. The amount detected in the troposphere is in the same range as the amounts detected with the ERICA-AMS during the cold and warm period of ND-MAX (Fig. 3). However, the stratospheric values were half of the values detected during the cold period in ND-MAX, probably due to the absence of BB material (regarding the warm period, no data referring to the LMS are available). Sulfate was found to be 0.1 $\mu g\,m^{-3}$ within the troposphere, before increasing to 0.7 $\mu g\,m^{-3}$ at approximately 14 km. During the cold (warm) period of ND-

MAX, tropospheric sulfate values were measured in a range of 0.02 to 0.08 µg m^{-3} (0.07 to 0.19 µg m^{-3}) and increased to 0.6 µg m^{-3} at 9 km under stratospheric influence (increased to ∼0.3 µg m^{-3} in the UT during the warm period) . Thus, the sulfate values of ND-MAX are in a comparable range to those detected during CAFE-Brazil. The ammonium concentration of CAFE-Brazil measurements remained below 0.05 µg m^{-3} up to 10 km before slightly rising to 0.07 µg m^{-3} at higher altitudes. Concentrations of $\mathrm{NH_4}$ were also detected during ND-MAX but the values often were below the detection limit of the ERICA-AMS (Fig. S19). The few data points, that exceeded the detection limit during the cold (warm) period, resulted in a concentration of 0.12 to 0.20 µg m^{-3} (0.12 to 0.15 µg m^{-3}) throughout the FT and LMS. Further, the nitrate concentration during CAFE-Brazil was below 0.01 µg m^{-3} up to 7 km. Above this altitude it continuously increased up to 0.09 µg m^{-3} at an altitude of 13 km. During the cold period ND-MAX, the $\mathrm{NO_3}$ concentration varied between 0.02 and 0.06 µg m^{-3} in the FT and LMS, covering the same range as during CAFE-Brazil. During the warm period, values above the detection limit were only obtained at around 12 km of ∼0.06 µg m^{-3}, consistent with the range measured during CAFE-Brazil. The chloride concentration measured during CAFE-Brazil was below 0.01 µg m^{-3} throughout the FT and LS and, thus, in the same range as the chloride values of 0.03 µg m^{-3} in the FT and 0.02 µg m^{-3} in the LMS obtained within the cold and warm period of ND-MAX. In conclusion, the ERICA-AMS provided mass concentrations of particulate organics, sulfate, ammonium, nitrate, and chloride for the UTLS region over Germany in winter that coincided with measurements of a C-ToF-AMS of a similar working principle.

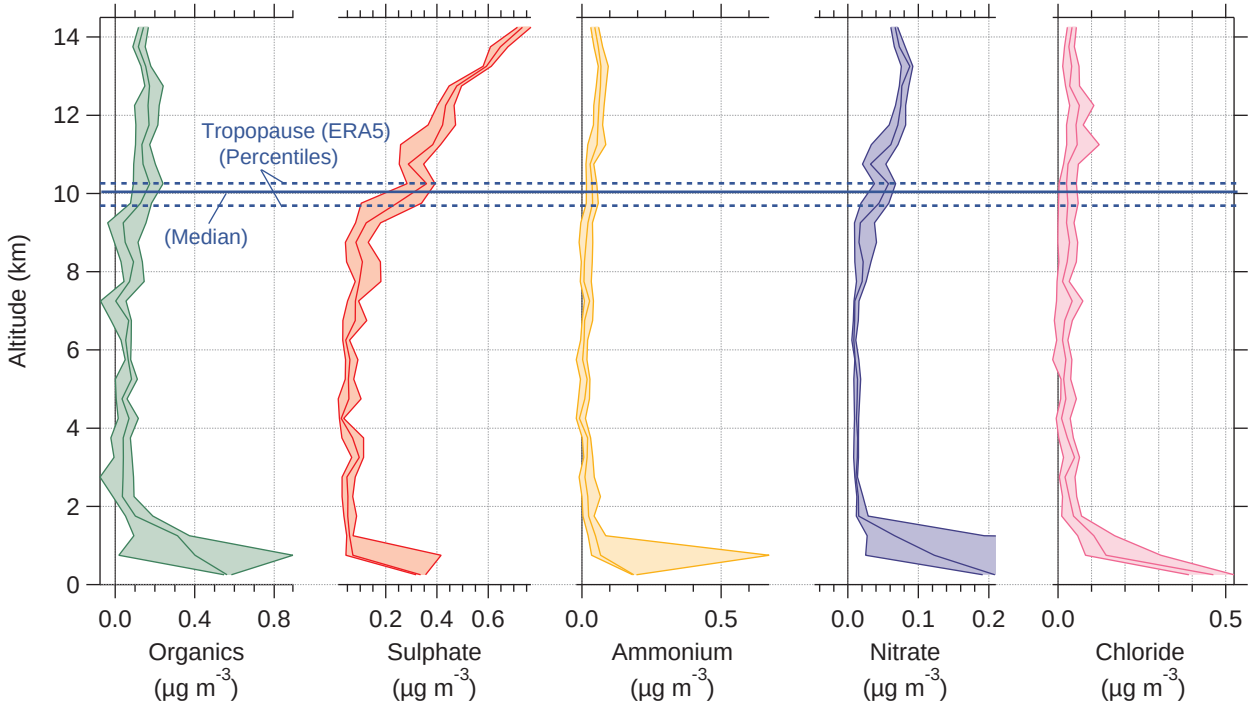

Figure S18. Mass concentrations of particulate organics (green), sulfate (red), ammonium (orange), nitrate (blue), and chloride (pink) obtained by the C-ToF-AMS (Schulz et al., 2018) as a function of GPS altitude. The vertical profiles are averaged over two test flights conducted in late November 2022 and two transfer flights conducted in late November 2022 and January 2023. The thick line and the shaded area represent the median and quartiles, respectively, in the corresponding altitude bin of 500 m width. The horizontal lines indicate the tropopause median and quartiles derived from ERA5 data for the considered flights (Hersbach et al., 2018).

S7 Uncertainty analysis

The particle fraction (PF) of individual particle types is estimated as the number of particles of an individual particle type (N_{type}) per number of all particles (N_{total}):

$$PF = \frac{N_{type}}{N_{total}} \tag{S4}$$

Using binomial statistics, the absolute uncertainty of the ERICA-LAMS particle fraction for each bin (σ_{PF}^{bin}) is calculated:

$$\sigma_{PF}^{bin} = \frac{\sqrt{N_{hits} \cdot PF \cdot (1 - PF)}}{N_{hits}} \tag{S5}$$

with the number of successfully ionized particles (N_{hits}) by the ablation laser of the ERICA-LAMS and the particle fraction of the respective particle type (PF) (e.g., Köllner et al., 2017, 2021; Appel et al., 2022). The source fractions of trajectories and corresponding errors are calculated analogously to PF.

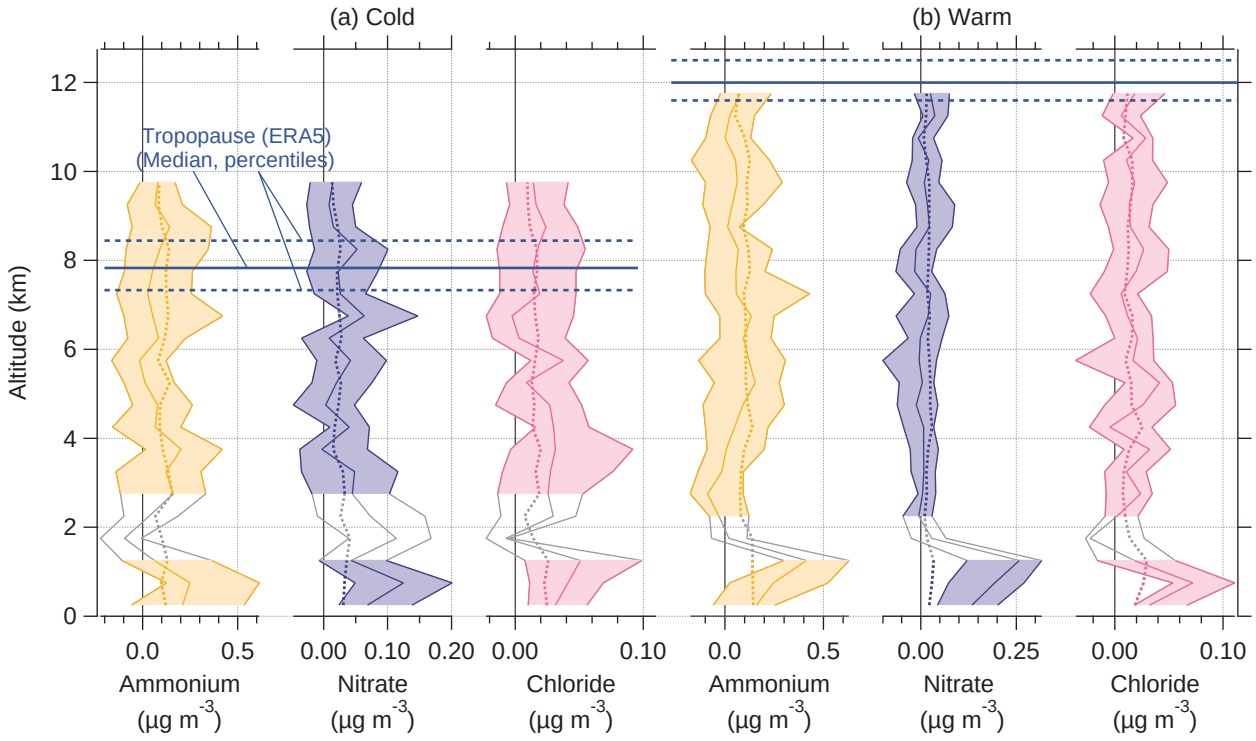

Figure S19. Vertical profiles of mass concentrations of particulate ammonium (orange), nitrate (blue), and chloride (pink) obtained by the ERICA-AMS as a function of GPS altitude for the cold period (a: RF1, RF2, and RF8) and warm period (b: RF3 and RF4) of the ND-MAX campaign 2018, binned in 500 m steps. The solid line and the shaded area represent the median and quartiles. For each altitude bin and substance the detection limit is displayed as a dotted line. The altitude range between 1.5 and 2.5 km in the cold period (between 1.5 and 2.0 km in the warm period) is not shaded since these bins comprise low counting statistics, i.e. less than 10 counts per bin. The horizontal lines indicate the tropopause median and quartiles derived from ERA5 data for the cold and warm period (Hersbach et al., 2018).

References

Angelino, S., Suess, D., and Prather, K.: Formation of Aerosol Particles from Reactions of Secondary and Tertiary Alkylamines: Characterization by Aerosol Time-of-Flight Mass Spectrometry, Environmental Science & Technology, 35, 3130–3138, https://doi.org/10.1021/es0015444, 2001.

Appel, O., Köllner, F., Dragoneas, A., Hünig, A., Molleker, S., Schlager, H., Mahnke, C., Weigel, R., Port, M., Schulz, C., Drewnick, F., Vogel, B., Stroh, F., and Borrmann, S.: Chemical analysis of the Asian tropopause aerosol layer (ATAL) with emphasis on secondary aerosol particles using aircraft-based in situ aerosol mass spectrometry, Atmospheric Chemistry and Physics, 22, 13 607–13 630, https://doi.org/10.5194/acp-22-13607-2022, 2022.

Bezdek, J. C., Ehrlich, R., and Full, W.: FCM: The fuzzy c-means clustering algorithm, Computers & Geosciences, 10, 191–203, https://doi.org/10.1016/0098-3004(84)90020-7, 1984.

Brauner, P.: Airborne measurements of the UTLS aerosol chemical composition over Germany using particle mass spectrometry, Ph.D. thesis, https://doi.org/10.25358/OPENSCIENCE-10892, 2024.

Canagaratna, M., Jayne, J., Jimenez, J., Allan, J., Alfarra, M., Zhang, Q., Onasch, T., Drewnick, F., Coe, H., Middlebrook, A., Delia, A., Williams, L., Trimborn, A., Northway, M., DeCarlo, P., Kolb, C., Davidovits, P., and Worsnop, D.: Chemical and microphysical characterization of ambient aerosols with the aerodyne aerosol mass spectrometer, Mass Spectrometry Reviews, 26, 185–222, https://doi.org/https://doi.org/10.1002/mas.20115, 2007.

Clemen, H.-C. et al.: Indications for non-soot aircraft emissions in cloud residuals and aerosol particles, in prep. for Atmospheric Chemistry and Physics, in prep.

Cornwell, G. C., Sultana, C. M., Prank, M., Cochran, R. E., Hill, T. C. J., Schill, G. P., DeMott, P. J., Mahowald, N., and Prather, K. A.: Ejection of Dust From the Ocean as a Potential Source of Marine Ice Nucleating Particles, Journal of Geophysical Research: Atmospheres, 125, https://doi.org/10.1029/2020JD033073, 2020.

Dragoneas, A., Molleker, S., Appel, O., Hünig, A., Böttger, T., Hermann, M., Drewnick, F., Schneider, J., Weigel, R., and Borrmann, S.: The realization of autonomous, aircraft-based, real-time aerosol mass spectrometry in the upper troposphere and lower stratosphere, Atmospheric Measurement Techniques, 15, 5719–5742, https://doi.org/10.5194/amt-15-5719-2022, 2022.

Drewnick, F., Hings, S. S., DeCarlo, P., Jayne, J. T., Gonin, M., Fuhrer, K., Weimer, S., Jimenez, J. L., Demerjian, K. L., Borrmann, S., and Worsnop, D. R.: A New Time-of-Flight Aerosol Mass Spectrometer (TOF-AMS)—Instrument Description and First Field Deployment, Aerosol Science and Technology, 39, 637–658, https://doi.org/10.1080/02786820500182040, 2005.

Gallavardin, S., Lohmann, U., and Cziczo, D.: Analysis and differentiation of mineral dust by single particle laser mass spectrometry, International Journal of Mass Spectrometry, 274, 56–63, https://doi.org/10.1016/j.ijms.2008.04.031, 2008.

Gunsch, M. J., May, N. W., Wen, M., Bottenus, C. L. H., Gardner, D. J., VanReken, T. M., Bertman, S. B., Hopke, P. K., Ault, A. P., and Pratt, K. A.: Ubiquitous influence of wildfire emissions and secondary organic aerosol on summertime atmospheric aerosol in the forested Great Lakes region, Atmospheric Chemistry and Physics, 18, 3701–3715, https://doi.org/10.5194/acp-18-3701-2018, 2018.

Healy, R. M., Evans, G. J., Murphy, M., Sierau, B., Arndt, J., McGillicuddy, E., O'Connor, I. P., Sodeau, J. R., and Wenger, J. C.: Single-particle speciation of alkylamines in ambient aerosol at five European sites, Analytical and Bioanalytical Chemistry (2015), 407, 5899–5909, https://doi.org/10.1007/s00216-014-8092-1, 2015.

Hersbach, H., Bell, B., Berrisford, P., Biavati, G., Horányi, A., Muñoz Sabater, J., Nicolas, J., Peubey, C., Radu, R., Rozum, I., Schepers, D., Simmons, A., Soci, C., Dee, D., and Thépaut, J.-N.: ERA5 hourly data on pressure levels from 1940 to present, https://doi.org/10.24381/cds.bd0915c6, 2018.

Hinz, K.-P., Kaufmann, R., and Spengler, B.: Laser-Induced Mass Analysis of Single Particles in the Airborne State, Analytical Chemistry, 66, 2071–2076, https://doi.org/10.1021/ac00085a023, 1994.

Hinz, K. P., Greweling, M., Drews, F., and Spengler, B.: Data processing in on-line laser mass spectrometry of inorganic, organic, or biological airborne particles, Journal of the American Society for Mass Spectrometry, 10, 648–660, https://doi.org/10.1016/S1044-0305(99)00028-8, 1999.

Hünig, A.: Development, characterization, and first field deploymentsof a novel aerosol mass spectrometer combining laserablation and flash vaporization techniques for aircraftapplication at high altitudes, phdthesis, Johannes Gutenberg Universität, https://doi.org/10.25358/openscience-5554, 2020.

Hünig, A., Appel, O., Dragoneas, A., Molleker, S., Clemen, H.-C., Helleis, F., Klimach, T., Köllner, F., Böttger, T., Drewnick, F., Schneider, J., and Borrmann, S.: Design, characterization, and first field deployment of a novel aircraft-based aerosol mass spectrometer combining

the laser ablation and flash vaporization techniques, Atmospheric Measurement Techniques, 15, 2889–2921, https://doi.org/10.5194/amt-15-2889-2022, 2022.

Johnston, M. V. and Wexler, A. S.: MS of INDIVIDUAL AEROSOL PARTICLES, Analytical Chemistry, 67, 721A–726A, https://doi.org/10.1021/ac00119a722, 1995.

Kellner, R., Mermet, J.-M., Otto, M., Valcárcel, M., and Widmer, H.: Analytical chemistry: a modern approach to analytical science, Wiley-VCH, 2004.

Köllner, F., Schneider, J., Willis, M. D., Klimach, T., Helleis, F., Bozem, H., Kunkel, D., Hoor, P., Burkart, J., Leaitch, W. R., Aliabadi, A. A., Abbatt, J. P. D., Herber, A. B., and Borrmann, S.: Particulate trimethylamine in the summertime Canadian high Arctic lower troposphere, Atmospheric Chemistry and Physics, 17, 13 747–13 766, https://doi.org/10.5194/acp-17-13747-2017, 2017.

Köllner, F., Schneider, J., Willis, M. D., Schulz, H., Kunkel, D., Bozem, H., Hoor, P., Klimach, T., Helleis, F., Burkart, J., Leaitch, W. R., Aliabadi, A. A., Abbatt, J. P. D., Herber, A. B., and Borrmann, S.: Chemical composition and source attribution of sub-micrometre aerosol particles in the summertime Arctic lower troposphere, Atmospheric Chemistry and Physics, 21, 6509–6539, https://doi.org/10.5194/acp-21-6509-2021, 2021.

Lee, S.-H., Murphy, D. M., Thomson, D. S., and Middlebrook, A. M.: Chemical components of single particles measured with Particle Analysis by Laser Mass Spectrometry (PALMS) during the Atlanta SuperSite Project: Focus on organic/sulfate, lead, soot, and mineral particles, Journal of Geophysical Research: Atmospheres, 107, AAC 1–1–AAC 1–13, https://doi.org/10.1029/2000JD000011, 2002.

Moffet, R. C. and Prather, K. A.: In-situ measurements of the mixing state and optical properties of soot with implications for radiative forcing estimates, Proceedings of the National Academy of Sciences, 106, 11 872–11 877, https://doi.org/10.1073/pnas.0900040106, 2009.

Molleker, S., Helleis, F., Klimach, T., Appel, O., Clemen, H.-C., Dragoneas, A., Gurk, C., Hünig, A., Köllner, F., Rubach, F., Schulz, C., Schneider, J., and Borrmann, S.: Application of an O-ring pinch device as a constant-pressure inlet (CPI) for airborne sampling, Atmospheric Measurement Techniques, 13, 3651–3660, https://doi.org/10.5194/amt-13-3651-2020, 2020.

Murphy, D. M.: The design of single particle laser mass spectrometers, Mass Spectrometry Reviews, 26, 150–165, https://doi.org/https://doi.org/10.1002/mas.20113, 2007.

Murphy, D. M. and Koop, T.: Review of the vapour pressures of ice and supercooled water for atmospheric applications, Quarterly Journal of the Royal Meteorological Society, 131, 1539–1565, https://doi.org/10.1256/qj.04.94, 2005.

Murphy, D. M. and Thomson, D. S.: Laser Ionization Mass Spectroscopy of Single Aerosol Particles, Aerosol Science and Technology, 22, 237–249, https://doi.org/10.1080/02786829408959743, 1995.

Ng, N. L., Canagaratna, M. R., Zhang, Q., Jimenez, J. L., Tian, J., Ulbrich, I. M., Kroll, J. H., Docherty, K. S., Chhabra, P. S., Bahreini, R., Murphy, S. M., Seinfeld, J. H., Hildebrandt, L., Donahue, N. M., DeCarlo, P. F., Lanz, V. A., Prévôt, A. S. H., Dinar, E., Rudich, Y., and Worsnop, D. R.: Organic aerosol components observed in Northern Hemispheric datasets from Aerosol Mass Spectrometry, Atmospheric Chemistry and Physics, 10, 4625–4641, https://doi.org/10.5194/acp-10-4625-2010, 2010.

Ng, N. L., Canagaratna, M. R., Jimenez, J. L., Chhabra, P. S., Seinfeld, J. H., and Worsnop, D. R.: Changes in organic aerosol composition with aging inferred from aerosol mass spectra, Atmospheric Chemistry and Physics, 11, 6465–6474, https://doi.org/10.5194/acp-11-6465-2011, 2011.

Prather, K. A., Nordmeyer, T., and Salt, K.: Real-time characterization of individual aerosol particles using time-of-flight mass spectrometry, Analytical Chemistry, 66, 1403–1407, https://doi.org/10.1021/ac00081a007, 1994.

Prather, K. A., Bertram, T. H., Grassian, V. H., Deane, G. B., Stokes, M. D., DeMott, P. J., Aluwihare, L. I., Palenik, B. P., Azam, F., Seinfeld, J. H., Moffet, R. C., Molina, M. J., Cappa, C. D., Geiger, F. M., Roberts, G. C., Russell, L. M., Ault, A. P., Baltrusaitis, J., Collins, D. B.,

Corrigan, C. E., Cuadra-Rodriguez, L. A., Ebben, C. J., Forestieri, S. D., Guasco, T. L., Hersey, S. P., Kim, M. J., Lambert, W. F., Modini, R. L., Mui, W., Pedler, B. E., Ruppel, M. J., Ryder, O. S., Schoepp, N. G., Sullivan, R. C., and Zhao, D.: Bringing the ocean into the laboratory to probe the chemical complexity of sea spray aerosol, Proceedings of the National Academy of Sciences, 110, 7550–7555, https://doi.org/10.1073/pnas.1300262110, 2013.

Pratt, K. A., Mayer, J. E., Holecek, J. C., Moffet, R. C., Sanchez, R. O., Rebotier, T. P., Furutani, H., Gonin, M., Fuhrer, K., Su, Y., Guazzotti, S., and Prather, K. A.: Development and Characterization of an Aircraft Aerosol Time-of-Flight Mass Spectrometer, Analytical Chemistry, 81, 1792–1800, https://doi.org/10.1021/ac801942r, 2009.

Schneider, J., Weigel, R., Klimach, T., Dragoneas, A., Appel, O., Hünig, A., Molleker, S., Köllner, F., Clemen, H.-C., Eppers, O., Hoppe, P., Hoor, P., Mahnke, C., Krämer, M., Rolf, C., Grooß, J.-U., Zahn, A., Obersteiner, F., Ravegnani, F., Ulanovsky, A., Schlager, H., Scheibe, M., Diskin, G. S., DiGangi, J. P., Nowak, J. B., Zöger, M., and Borrmann, S.: Aircraft-based observation of meteoric material in lower-stratospheric aerosol particles between 15 and 68° N, Atmospheric Chemistry and Physics, 21, 989–1013, https://doi.org/10.5194/acp-21-989-2021, 2021.

Schulz, C., Schneider, J., Amorim Holanda, B., Appel, O., Costa, A., de Sá, S. S., Dreiling, V., Fütterer, D., Jurkat-Witschas, T., Klimach, T., Knote, C., Krämer, M., Martin, S. T., Mertes, S., Pöhlker, M. L., Sauer, D., Voigt, C., Walser, A., Weinzierl, B., Ziereis, H., Zöger, M., Andreae, M. O., Artaxo, P., Machado, L. A. T., Pöschl, U., Wendisch, M., and Borrmann, S.: Aircraft-based observations of isoprene-epoxydiol-derived secondary organic aerosol (IEPOX-SOA) in the tropical upper troposphere over the Amazon region, Atmospheric Chemistry and Physics, 18, 14 979–15 001, https://doi.org/10.5194/acp-18-14979-2018, 2018.

Silva, P. J., Carlin, R. A., and Prather, K. A.: Single particle analysis of suspended soil dust from Southern California, Atmospheric Environment, 34, 1811–1820, https://doi.org/10.1016/S1352-2310(99)00338-6, 2000.

Su, B., Bi, X., Zhang, Z., Liang, Y., Song, C., Wang, T., Hu, Y., Li, L., Zhou, Z., Yan, J., Wang, X., and Zhang, G.: Enrichment of calcium in sea spray aerosol: insights from bulk measurements and individual particle analysis during the R/V *Xuelong* cruise in the summertime in Ross Sea, Antarctica, Atmospheric Chemistry and Physics, 23, 10 697–10 711, https://doi.org/10.5194/acp-23-10697-2023, 2023.

Suess, D. T. and Prather, K. A.: Mass Spectrometry of Aerosols, Chemical Reviews, 99, 3007–3036, https://doi.org/10.1021/cr980138o, 1999.

Zelenyuk, A. and Imre, D.: Single Particle Laser Ablation Time-of-Flight Mass Spectrometer: An Introduction to SPLAT, Aerosol Science and Technology, 39, 554–568, https://doi.org/10.1080/027868291009242, 2005.